



Published in final edited form as:

Cell Rep. 2018 April 03; 23(1): 58–67. doi:10.1016/j.celrep.2018.03.032.

Mitochondrial Complex I Inhibitors Expose a Vulnerability for Selective Killing of *Pten*-Null Cells

Adam Naguib^{#1}, Grinu Mathew^{#1}, Colleen R. Reczek², Kaitlin Watrud¹, Alexandra Ambrico¹, Tali Herzka¹, Irene Casanova Salas¹, Matthew F. Lee¹, Nour El-Amine¹, Wu Zheng¹, M. Emilia Di Francesco³, Joseph R. Marszalek³, Darryl J. Pappin¹, Navdeep S. Chandel², and Lloyd C. Trotman^{1,5,*}

¹Cold Spring Harbor Laboratory, Cancer Biology, Cold Spring Harbor, NY, USA

²Northwestern Medical School, Cell and Molecular Biology, Chicago, IL, USA

³Institute for Applied Cancer Science, University of Texas, MD Anderson Cancer Center, Houston, TX, USA

These authors contributed equally to this work.

SUMMARY

A hallmark of advanced prostate cancer (PC) is the concomitant loss of PTEN and p53 function. To selectively eliminate such cells, we screened cytotoxic compounds on *Pten*^{-/-}; *Trp53*^{-/-} fibroblasts and their *Pten*-WT reference. Highly selective killing of *Pten*-null cells can be achieved by deguelin, a natural insecticide. Deguelin eliminates *Pten*-deficient cells through inhibition of mitochondrial complex I (CI). Five hundred-fold higher drug doses are needed to obtain the same killing of *Pten*-WT cells, even though deguelin blocks their electron transport chain equally well. Selectivity arises because mitochondria of *Pten*-null cells consume ATP through complex V, instead of producing it. The resulting glucose dependency can be exploited to selectively kill *Pten*-null cells with clinically relevant CI inhibitors, especially if they are lipophilic. *In vivo*, deguelin suppressed disease in our genetically engineered mouse model for metastatic PC. Our data thus introduce a vulnerability for highly selective targeting of incurable PC with inhibitors of CI.

Graphical Abstract

This is an open access article under the CC BY-NC-ND license (<http://creativecommons.org/licenses/by-nc-nd/4.0/>).

*Correspondence: trotman@cshl.edu.

⁵Lead Contact

AUTHOR CONTRIBUTIONS

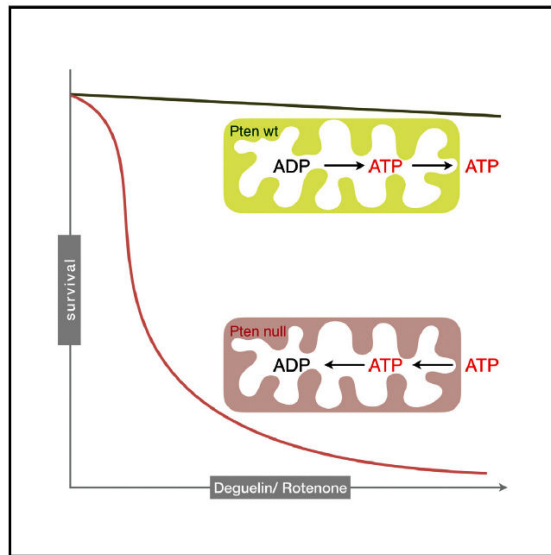
A.N., G.M., C.R.R., E.D.F., J.R.M., D.J.P., N.C.S., and L.C.T. designed the study. A.N., G.M., C.R.R., K.W., A.A., T.H., I.C.S., M.F.L., N.A., and W.Z. performed experiments. A.N., G.M., N.S.C., and L.C.T. wrote the manuscript.

DECLARATION OF INTERESTS

The authors declare no competing interests.

SUPPLEMENTAL INFORMATION

Supplemental Information includes STAR Methods and four figures and can be found with this article online at <https://doi.org/10.1016/j.celrep.2018.03.032>.



Naguib et al. find that *Pten*-null cells are highly vulnerable to mitochondrial complex I inhibition under conditions in which *Pten*-WT cells remain perfectly viable. They suggest that such an approach could serve as a blueprint for selective targeting of lethal *Pten*-deficient metastatic prostate cancer.

INTRODUCTION

Today, we understand cancer as a stepwise progression in malignant phenotype of cells, combined with non-cell-autonomous failures to halt progression of disease. The past decade has seen huge progress in the genetic characterization of deadly cancers (reviewed in Garraway and Lander, 2013). Major emerging principles are the high complexity and subclonal diversification (branching) found within one as well as between metastatic sites (for examples, see Gudem et al., 2015; Wang et al., 2014). Another emerging principle is that both bulk tumor analysis and single-cell resolution studies point to a single cell of origin, whose descendants periodically overcome distinct bottlenecks for progression. One such bottleneck is the overcoming of the p53-induced cellular senescence program. This is triggered by the complete loss of *PTEN*, as identified in pre-clinical cancer models and human cancer cells (Alimonti et al., 2010; Chen et al., 2005; Ding et al., 2011; Kim et al., 2006). In agreement, whole-genome analysis of human prostate cancer shows that co-deletion of *PTEN* and *TP53* is associated with highly advanced and metastatic disease (Chen et al., 2011; Robinson et al., 2015; Taylor et al., 2010). On the basis of these reports, 20% co-alteration is seen in the 17% of patients who have distant and locally advanced PC. This would suggest that of the 3 million American men with PC, roughly 100,000 carry cancers with co-mutation of these genes.

We have recently validated the lethal and metastatic nature of this genotype by showing causality in a pre-clinical PC model called RapidCaP. This genetically engineered mouse (GEM) model is highly prone to develop metastasis and resistance to hormone deprivation, the standard of care in advanced PC (Cho et al., 2014). This prompted us to screen for drugs

against this specific genotype. Importantly, several studies revealed that p53 loss alone led to no signs of prostate disease (Chen et al., 2005; Ding et al., 2011). We thus set out to identify drugs that selectively target genetically engineered cells of the genotype that gives rise to lethal disease (*Pten*^{-/-}; *Trp53*^{-/-}) while sparing the cells that show no prostate phenotype (*Trp53*^{-/-}; see Figure 1A).

RESULTS

Pten-Null Cells Are Selectively Killed by Deguelin and Rotenone

To test for compounds, we used the OmniLog Biolog platform (<http://www.biolog.com>), which combines drug-coated 96-well plates with a dedicated cell incubator/spectrophotometer for continuous measurement of viability as the system reads accumulation of a tetrazolium-based dye for 24 hr at 15 min intervals. We screened a total of 23 cytotoxic drugs that include known chemotherapy agents and thus obtained viability curves for each cell type at four concentrations per drug. Without drug, *Pten*-null cells showed a higher dye turnover, consistent with faster growth that we have described previously (Chen et al., 2005; Nowak et al., 2015). First, a qualitative overview of the results showed that several known chemotherapy agents indiscriminately reduced viability of both cell types, as seen with representative concentrations of, for example, the thymidylate synthase inhibitor 5'-fluorouracil (5-FU) and the anthracycline aclarubicin or the microtubule-stabilizing agent docetaxel compared with no treatment (Figure 1B; see also Figure S2F for docetaxel). As shown in Figure 1C, the readout produced by the Biolog system facilitated the comparison of drug effects on the cells by indicating as a green curve segment the amount by which the *Pten*-null cells are more viable than the wild-type (WT) cells, which are shown as a yellow curve. Evaluating the overview of the drug effects on the two cell types, we found that two compounds selectively reduced activity of *Pten*-null cells, as indicated by the appearance of a red curve segment, showing the amount by which the *Pten*-deficient cells showed less viability than their WT counterparts. Quantification of half maximal inhibitory concentration (IC₅₀) values for each drug and ranking by the ratio of IC₅₀ in *Pten*-null to that in *Pten*-WT cells revealed that none of the chemotherapy agents selectively targeted the faster growing *Pten*-deficient cells, while the two drugs rotenone and deguelin did (Figure 1D, bottom; see also Experimental Procedures). Curve comparison in Figure 1E shows how deguelin selectively targeted the *Pten*-null cells.

Deguelin Kills *Pten*-Null Cells by Inhibition of Mitochondrial Complex I

Rotenone is a potent inhibitor of mitochondrial complex I (CI) that is present in a root extract called cube resin, which has been widely used as potent insecticide and fish poison (Fang and Casida, 1998). Deguelin, another component of this extract, has a similar structure (Figure S1B) and was found to be less toxic than rotenone in mice (Caboni et al., 2004), which is why we selected it for further analysis. Deguelin can be synthesized from rotenone (Anzeveno, 1979), most recently in three steps (Caboni et al., 2004; Figure S1B). To test if deguelin targets *Pten*-null cells through mitochondrial inhibition, we performed a series of tests. First, we determined the drug's effect on mitochondrial morphology by MitoTracker staining. Super-resolution confocal microscopy revealed massive mitochondrial fragmentation upon deguelin treatment (Figures 2A and S1C), a hallmark of CI inhibition by

rotenone (see, e.g., Barsoum et al., 2006). Quantification showed that deguelin caused the fragmentation in both *Pten*-WT and null cells (note that microtubule [MT] lengths between the two genotypes were indistinguishable). Next, we tested the effect of deguelin on oxygen consumption rate (OCR). As shown in Figure 2B, deguelin strongly blocked OCR at various concentrations. We then dissected the effect on components of the electron transport chain (ETC) by testing cells after permeabilization and found that deguelin inhibits CI contribution to respiration, but not that of complex II (Figure 2B, complex II). These results showed that deguelin acts on CI. Several recent reports argued that deguelin acts by suppressing a multitude of signaling pathways, including PI 3-kinase/Akt (reviewed in Wang et al., 2013), whereas in contrast, binding studies indicated accumulation in MTs (Garcia et al., 2012). Therefore, we next tested if its inhibition of CI was both essential and sufficient for killing of the *Pten*-null cells. A hallmark of ETC inhibition is that it can be overcome by glucose, which allows cells to produce ATP through glycolysis. As shown (Figure S2A), raising the glucose concentration from physiological 7 mM to 25 mM, which is often used in tissue culture, caused a reduction of killing by deguelin from 90% to 9%. We next asked if restoration of CI function is sufficient to rescue this killing. To this end we expressed the yeast NDI1 transgene, which can drive electron flux in the ETC (Wheaton et al., 2014) but is insensitive to CI inhibitors, including rotenone (Seo et al., 1998). As shown in Figure 2C, expression of NDI1 rescued respiration in the presence of deguelin close to normal levels, while at the same time NDI1 on its own did not increase OCR in the *Pten*-null cells. Next we tested the effect on cell killing using propidium iodide as readout. By performing this rescue experiment in galactose, we furthermore enforced the condition that no net ATP production stem from glycolysis. As shown in Figure 2D, yeast NDI1 rescued the viability of deguelin treated *Pten*-null cells, while NDI1 alone did not increase viability of cells in galactose. When assayed in 25 mM glucose, NDI1 had no effect on cell viability, while cells became resistant to deguelin-mediated killing (consistent with Figure S2A). Note that Figure 2C measures mitochondrial OCR, which reveals CI inhibition and rescue irrespective of glucose levels, whereas Figure 2D measures cell viability, which does respond to glucose levels because of contribution from glycolysis. Taken together, these results showed that inhibition of mitochondrial CI is the necessary and sufficient action of deguelin through which it preferentially kills the *Pten*-null cells.

Complex V Function Is Reversed in *Pten*-Null Cells

When testing deguelin in *Pten*-WT cells, we confirmed that it had the same effects as seen in *Pten*-null cells (Figure S2B): deguelin blocked OCR in both intact and permeabilized cells, and it also inhibited mitochondrial CI, not complex II. Therefore, we next asked how deguelin can preferentially target *Pten*-deficient cells. Our results suggested that the ETC components downstream of CI, namely, complex III and complex IV, were equally affected in both genotypes. We next tested if complex V, which imports protons back into the matrix to produce ATP (Figure S2C), behaves differently in the two genotypes. As shown (Figure 3A), inhibition of complex V resulted in a 3.5-fold increase of mitochondrial membrane potential of WT cells at high glucose (25 mM). At 7 mM glucose, this increase in membrane potential was still significant, albeit lower, as expected (see Figures 3A and S2D). Thus, we could infer that mitochondria of these cells are generating more or less ATP as a function of glucose concentrations. When testing the *Pten*-null cells, we also saw increased membrane

potential upon complex V inhibition at 25 mM glucose. In contrast, however, membrane potential decreased when complex V was inhibited at 7 mM glucose. This indicated that at physiological glucose, complex V is not producing ATP coupled to proton import but instead is consuming ATP coupled to proton export from the matrix (see Figure 3A, cartoon). Complex V reversal is a known mechanism to preserve mitochondrial membrane potential at the cost of ATP consumption (Martínez-Reyes et al., 2016). We next validated this finding by using carboxyatractyloside (CATR) to examine the role of the adenine nucleotide translocator (ANT). ANT inhibition should prevent ATP/ADP exchange between cytoplasm and matrix and thus is expected to diminish complex V proton pumping activity (see Figure 3A, cartoon). Indeed, CATR treatment selectively reduced membrane potential in the *Pten*-null cells at 7 mM starting glucose, just like oligomycin did (Figure S2D). In WT cells, in contrast, ANT inhibition by CATR caused increased membrane potential, like oligomycin did. Our results indicate that effectively, the mitochondria of the *Pten*-deficient cell are turned into ATP consumers, thus generating a high dependence on ATP production through glycolysis.

Deguelin Targets the Glucose/ATP Dependence of *Pten*-Null Cells

Finally, we sought to test if CI inhibitors kill *Pten*-deficient cells by exploiting the fact that mitochondrial ATP consumption causes glucose to become limiting. First, we tested deguelin-mediated cell killing over 24 hr as a function of starting glucose concentration in the medium (Figure 3B). This revealed preferential targeting of *Pten*-null cells in the range of 5–10 mM starting glucose, which roughly represents the physiological diurnal-to-nocturnal range. Most important, the selective effect on *Pten*-null cells narrows as starting glucose is increased, and the effect is completely lost at 25 mM starting glucose. This was in stark contrast to the clinically relevant chemotherapy agent used in PC, docetaxel: it killed the cells irrespective of *Pten* status or glucose concentration (Figure S2F). Together, our results suggested that deguelin could accelerate the high need for glucose of *Pten*-null cells, more than that of the *Pten*-WT cells, thus leading to selective killing due to faster glucose depletion. To test this hypothesis, we compared medium glucose depletion in both cell types. As shown in Figure 3C, the untreated *Pten*-null cells depleted more glucose per cell than the *Pten*-WT over a 20 hr period, as expected. Addition of deguelin, however, led to an increase in glucose consumption in the *Pten*-null cells, even though deguelin blocked cell proliferation. Overall, we observed a 29-fold difference in per cell glucose consumption when comparing the two genotypes after 20 hr. These results confirmed the hypothesis that selective killing of deguelin occurs because of its shortened time to glucose depletion in the *Pten*-null cells.

Inhibitor Properties Dictate the Maximal Achievable Window for Selective Killing

Taken together, our data pointed toward a strategy for selective killing the *Pten*-deficient cells by forcing them into glucose consumption beyond what is available in order to maintain membrane potential. This hypothesis would then imply that maximizing the selective window for killing the *Pten*-deficient cells is a function of time and drug concentration. We first tested this hypothesis with deguelin. As shown in Figure 3D, a massive window (467-fold difference) of genotype-selective killing is seen at 48 hr post-treatment, not at 24 hr. As seen by the kill curves, the longer exposure results in death of

Pten-null cells below 10 nM deguelin concentrations, but not the WT, consistent with the hypothesis. We next tested rotenone and found that although the same principle applied, the optimal window of selective killing was seen at 24 hr instead. This immediately suggested very different ideal administration modes for the two highly related drugs. After 48 hr of rotenone treatment, we observed only a minor genotype-selective window because of effective killing of WT cells. Because no difference between the efficacy of these two drugs on CI inhibition was measured (see also Akatsuka et al., 2016), our results suggested that differences in their transport to the site of action translate into different kinetics for achieving maximal genotype selectivity.

We therefore expanded this analysis to a selection of clinically relevant CI inhibitors. As summarized in Figure S3A, we first tested the common anti-diabetic agent metformin. It showed little genotype selectivity over the time frame of 24–72 hr and precipitated at highest concentrations. Because this biguanide compound is positively charged, it is thought to be self-limiting because its uptake into mitochondria depends on membrane potential, which it suppresses (Chandel et al., 2016). Phenformin is a more lipophilic aromatic derivative of metformin (Figure S3A), resulting in ~10 times faster uptake in cells (Sogame et al., 2009), and it possesses different pharmacological properties (reviewed in Pernicova and Korbonits, 2014). Phenformin indeed showed some genotype-selective killing at 24 and 48 hr, which is consistent with the notion that it may still reach target when membrane potential is low, but it only affected less than half of the cells (Figure S3A). The selective kill window was lost by 72 hr, when 100% of both cell genotypes were affected. Next, we tested IACS-010759, a CI inhibitor that was developed recently and is currently in clinical trials for acute myeloid leukemia (AML) ([ClinicalTrials.gov](https://clinicaltrials.gov/ct2/show/study/NCT02882321) identifier NCT02882321; see also Baran et al., 2016). IACS-010759 showed optimal genotype selectivity at around 48 hr and affected 100% of the cells at the clinically relevant concentration of 100 nM.

Taken together, these results were consistent with the hypothesis that time to glucose depletion acts as a filter that can be used to optimize selective killing of the *Pten*-null cells. We confirmed this principle in PTEN-WT and mutant human PC cell lines and in RapidCaP derived primary prostate cancer cells (Figure S3B). Furthermore, we learned that changes in drug properties, which are assumed to affect transport to CI, dictate when exactly this filter best separates *Pten*-null from *Pten*-normal.

Deguelin Is Well Tolerated and Targets Lethal Prostate Cancer in Mice

Finally, we tested if the strong CI inhibitor deguelin can be used to fight advanced prostate cancer *in vivo*. First, we tested uptake of the drug in mouse prostate tissue after administration. Using liquid chromatography-mass spectrometry (LC-MS) to measure deguelin levels, we found that it could be successfully delivered. Tissue exposure in prostate peaked within 1 hr of administration. Partial clearance of deguelin was noted at the 2 hr time point, which then decreased steadily through the end of the experiment (6 hr post-injection). Next, we tested if deguelin hits its functional target in prostate. As shown above using tissue culture (see Figure 2A), CI inhibition by deguelin resulted in fragmentation of mitochondria. When testing mitochondrial morphology in treated prostates, we also found that the extended shape of normal mitochondria in control treated prostate (see Figure 4B, DMSO)

was lost in favor of weak stained, fragmented mitochondria in the epithelial cells (Figure 4B, deguelin, and Figure S3C). Figure S3C (deguelin, bottom) in particular revealed the outline of the epithelium and the weak staining of severed MTs by binary black-white enhancement of the mitochondrial Tom20 staining. Our combined analysis thus showed that deguelin (1) reached prostate at a pharmacologically relevant dose and (2) was able to hit its target in prostate epithelium.

We next tested the drug in our GEM model for lethal metastatic prostate cancer (PC), termed RapidCaP, which is based on somatic delivery of Cre-lentivirus to few prostate cells (Cho et al., 2014, 2015; Nowak et al., 2015). It is unique for allowing live imaging and therapy of endogenous lethal metastatic PC, triggered by co-deletion of *Pten* and *Trp53*, a prominent clinical genotype of lethal human PC (Chen et al., 2011; Robinson et al., 2015; Taylor et al., 2010). As shown in Figure 4C, bioluminescence luciferase imaging (BLI) revealed both primary and secondary disease in pre-treatment animals. Given the previously published toxicity in mice (Caboni et al., 2004), we decided on a dose escalation schedule over a 10 week period (Figure S3D, cartoon), which is comparable with the time required for a therapeutic effect using castration therapy in RapidCaP (Cho et al., 2014). Quantification of weight change, an indicator of animal well-being, showed only 5% maximal weight loss over the 10 week trial period, indicating good tolerability of the drug and its dosing in animals with significant disease burden. BLI monitoring of the overall disease burden as a percentage relative to the starting point revealed the expected increase in the DMSO control animal, but (1) significant reduction in both primary and secondary disease of treated animals and (2) using Response Evaluation Criteria in Solid Tumors (RECIST) criteria (Therasse et al., 2000), stable disease (SD) and partial remission (PR) in the treated animals, compared with progressive disease (PD) in the control. Prostate immunofluorescence-immunohistochemistry (IF-IHC) analysis of Ki-67 revealed no glands with abnormal proliferation upon deguelin treatment (Figure 4D). Furthermore, we performed total thin-section histologic analysis of prostate, sampling approximately every 40th section with histogenic markers. In agreement with the Ki-67 results, lesions were found in DMSO-treated prostate but not in deguelin-treated prostate (Figure S4A). Furthermore, analysis of normal prostate glands confirmed significantly lowered mitochondrial staining upon deguelin treatment, confirming drug function *in situ* (Figure S4A, Tom20 intensity). Collectively, our results showed that deguelin (1) is well tolerated over an extended period, (2) reaches prostate, (3) hits its target, and (4) can stall or revert progression of advanced PC, in line with early metformin trial results from human metastatic PC patients (Rothermundt et al., 2014).

DISCUSSION

Landmark studies have connected metformin use with reduced cancer mortality (Landman et al., 2010; Xu et al., 2015), spawning a number of clinical trials (as reviewed in Pernicova and Korbonits, 2014). In prostate specifically, a decrease in cancer mortality has been seen, but not in cancer incidence (Margel et al., 2013a, 2013b). This suggests that metformin may preferentially target aggressive PC, which is the subject of ongoing trials (Gillesen et al., 2016). The discovery of CI as the functional target of metformin (Wheaton et al., 2014) has

led to development of trials with more effective yet tolerated drugs, such as the IACS-010759 compound used in this study.

Our results can contribute to these efforts. They point to a mitochondrial vulnerability, driven by complex V inversion, for achieving highly selective killing of advanced *Pten*-deficient PC cells. They suggest that maximal selective killing by a given CI inhibitor is dependent on two completely intertwined factors: (1) depletion of tumor cell glucose supplies and (2) the inhibitor's properties of transport to the target. The first point should be critical in trial design: currently CI inhibitors such as metformin are given to PC patients with or just after meals (i.e., coinciding with highest plasma glucose levels), following the paradigm established for diabetes. Our results instead suggest that greater selectivity might be achieved if drugs are given when blood glucose levels are low. The second point should be critical for drug design: we found that changes in CI inhibitor properties critically affect the optimal time to achieve genotype-selective killing. This effect was most striking when comparing deguelin with rotenone (Figure 3C). Therefore, drug optimization could benefit from the type of time and genotype-selective approach on which our study is based.

EXPERIMENTAL PROCEDURES

Cell Lines and Culture—Creation of *Trp53*^{-/-} and *Trp53*^{-/-}/*Pten*^{-/-} mouse embryonic fibroblasts (MEFs) has been described previously (Chen et al., 2005). In brief, MEFs carrying the loxP flanked alleles of the genes were generated and subsequently infected with lentivirus encoding Cre-PURO-IRES-GFP and drug selected. Primary cell lines from RapidCaP mice were generated by collagenase digestion of the prostate. Cells (*Trp53*^{-/-}/*Pten*^{-/-}) were isolated by fluorescence-activated cell sorting (FACS) for TdTomato fluorescence. The pMIRW (MSCV-IRES-RFP-WPRE) vector or empty vector (EV) was generated by removing GFP from the pMIG plasmid (9044; AddGene) and replacing it with RFP-WPRE, PCR amplified from the pCDH-CMV-MCS-EF1-RFP plasmid (CD512B-1; System Biosciences). Further methods are described in the Supplemental Information.

Drug Screening—Twenty-three different chemotherapeutic compounds were tested for efficacy against MEFs of both genotypes. Tests were carried out in biological replicate. Screens were performed using OmniLog instruments and Phenotype Microarray technology (both from BioLog). Further methods are described in the Supplemental Information.

Cell Growth Curves and Treatments—MEFs were plated and incubated in DMEM (Mediatech), 10% fetal bovine serum (FBS), penicillin 50 U/mL (Sigma-Aldrich) streptomycin 100 µg/mL (Sigma-Aldrich) at 37°C, 5% CO₂, and 100% humidity. Medium was supplemented with DMSO (Sigma-Aldrich) at 0.1% or the indicated concentrations of deguelin (Cayman Chemical) from a stock solution in DMSO. At the indicated time points, cells were fixed and stained with crystal violet (Sigma-Aldrich), and absorbance at 590 nm was measured as a readout of cell number.

For MTT assays, cell viability assay was performed as per the kit guidelines. Ten thousand cells per well (96-well plate) grown in 7 mM glucose media were treated with the drug or DMSO for 24, 48, or 72 hr. Post-treatment, the cells were washed twice with PBS, and MTT solution was added. After labeling cells with MTT, the absorbance was read at 570 nM. All

experiments were performed as triplicates, and the relative cell viability was calculated as a percentage relative to the untreated control.

Mitochondrial Activity Studies—OCRs were measured using the XF24 Extracellular Flux Analyzer (Seahorse Bioscience). *Trp53*^{-/-} or *Trp53*^{-/-}/*Pten*^{-/-} MEFs were seeded onto 24-well Seahorse plates in complete media at a density of 4×10^4 cells/well 2 hr prior to OCR measurements. Detailed methods are described in the Supplemental Information.

Super-Resolution Microscopy and Quantification—*Pten*-WT or null cells grown on coverslips were stained with MitoTracker Red FM. Post-staining, high-resolution images of live stained or 4% paraformaldehyde-fixed cells were acquired using an OMX 3D structured illumination microscope (Applied Precision; see also Naguib et al., 2015). Quantification of maximal mitochondrial length was performed using ImageJ software (<https://imagej.nih.gov/ij/>). To measure mitochondrial length, all images were converted to 8-bit files. The straight line selection tool was used to trace the length of mitochondria in the entire cell.

RapidCaP Generation and Pre-clinical Trial—All protocols for mouse experiments were in accordance with institutional guidelines and approved by the Institutional Animal Care and Use Committee (IACUC). RapidCaP generation is mentioned in the Supplemental Information, and virus preparation and design for recombination of the *Trp53* and *Pten* loci has been described previously (Cho et al., 2014).

For pre-clinical trials, mice were treated with deguelin (Sigma-Aldrich) via intra-peritoneal injection on a Monday/Wednesday schedule. The dose of deguelin was escalated over the course of the trial, starting with 0.4 mg/kg and increasing to 1.6 mg/kg in 2 weeks. A dose of 1.2 mg/kg was determined to be effective, and mice were treated at 1.2 mg/kg until week 5 of the trial. The dose was then increased from 1.2 to 4 mg/kg (i.e., 1.6 mg/kg on Monday, 2.0 mg/kg on Wednesday) over the course of the remaining 5 weeks. Further methods for live imaging and deguelin dosing are described in the Supplemental Information.

Prostate Deguelin Extraction and LC Mass Spectrometry—Tissue was homogenized with 300 μ L of 1 \times PBS and sonicated for 60 s. Two hundred microliters of ethyl acetate was added to homogenates, followed by vortexing. Two hundred microliters were then transferred to a new tube and centrifuged at 14,000 rpm for 10 min. The ethyl acetate layer was transferred to a clean 1.7 mL tube and evaporated using a speed vac. Samples were reconstituted with 100 μ L of 50% acetonitrile with 0.1% formic acid, and 5 μ L were injected onto the triple-quadrupole mass spectrometer. Further mass spectrometry methods are described in the Supplemental Information.

Statistical Methods—Data were plotted and statistical analysis was performed using Numbers and GraphPad Prism. Plots are composed of the mean of minimally three data points, and error bars represent SD, unless noted otherwise. Statistical significance was determined using t tests, one-way ANOVA with Dunnett multiple comparisons, and two way ANOVA with Bonferroni multiple comparisons. Comparison of the slope of bioluminescence signal change over time in treated and untreated mice was done using a linear regression analysis.

Supplementary Material

Refer to Web version on PubMed Central for supplementary material.

ACKNOWLEDGMENTS

L.C.T. is a research scholar of the American Cancer Society and is supported by the Pershing Square Sohn Foundation and the U.S. Department of Defense (W81XWH-13-PCRP-IDA). This work was directly supported by grants to L.C.T. from the NIH (CA137050), the American Cancer Society (RSG-14-069-01-TBE), the Department of Defense (W81XWH-14-1-0247 and PC160647 to I.C.S.), the Robertson Research Fund of Cold Spring Harbor Laboratory, the Cold Spring Harbor Laboratory Cancer Center Support Grant from the NIH (5P30CA045508) to support the microscopy, flow cytometry, mass spectrometry, animal husbandry, and histologic analysis of this project and by grants from the NIH to N.S.C. (R35CA197532) and to C.R.R. (T32 HL076139–11). We would like to thank Drs. Lawrence A. Wiater, Serena Chan, and Elina Golder from Biolog for help with generation and analysis of the data; Dr. David. Tuveson for discussion of the results; Dr. Carla-Maria Gauss for help with chemistry; Dr. Larry Wiater for help with evaluation of the drug screen; Dr. Rachel Strittmatter and Lisa Bianco for help in execution and analysis of pre-clinical trials; and Keith Rivera for LC-MS analysis. We thank Aigoul Nourjanova, Denise Hoppe-Cahn, Kristin Milicich, and Dr. Qing Gao for help with histologic procedures and analysis; Pamela Moody for help with FACS procedures; and Dorothy Tsang and members of the Trotman lab for help with the manuscript.

REFERENCES

- Akatsuka A. Kojima N. Okamura M. Dan S. Yamori T. A novel thiophene-3-carboxamide analog of annonaceous acetogenin exhibits antitumor activity via inhibition of mitochondrial complex I *Pharmacol. Res. Perspect.* 2016; 4:e00246. [PubMed: 28116099]
- Alimonti A. Nardella C. Chen Z. Clohessy JG. Carracedo A. Trotman LC. Cheng K. Varmeh S. Kozma SC. Thomas G. A novel type of cellular senescence that can be enhanced in mouse models and human tumor xenografts to suppress prostate tumorigenesis *J. Clin. Invest.* 2010; 120:681. [PubMed: 20197621]
- Anzeveno PB. Rotenoid interconversion—synthesis of deguelin from rotenone *J. Org. Chem.* 1979; 44:2578.
- Baran N. Molina J. Cavazos A. Harutyunyan K. Feng N. Gay J. Piya S. ShanmugaVelandy S. Jabbour EJ. Andreeff M. Mitochondrial complex I inhibition with IACS-010759 in T-ALL preclinical models *Blood.* 2016; 128:4028.
- Barsoum MJ. Yuan H. Gerencser AA. Liot G. Kushnareva Y. Graber S. Kovacs I. Lee WD. Waggoner J. Cui J. Nitric oxide-induced mitochondrial fission is regulated by dynamin-related GTPases in neurons *EMBOJ.* 2006; 25:3900.
- Caboni P. Sherer TB. Zhang N. Taylor G. Na HM. Greenamyre JT. Casida JE. Rotenone, deguelin, their metabolites, and the rat model of Parkinson's disease *Chem. Res. Toxicol.* 2004; 17:1540. [PubMed: 15540952]
- Chandel NS. Avizonis D. Reczek CR. Weinberg SE. Menz S. Neuhaus R. Christian S. Haegerbarth A. Algire C. Pollak M. Are metformin doses used in murine cancer models clinically relevant? *Cell Metab.* 2016; 23:569. [PubMed: 27076070]
- Chen Z. Trotman LC. Shaffer D. Lin HK. Dotan ZA. Niki M. Koutcher JA. Scher HI. Ludwig T. Gerald W. Crucial role of p53-dependent cellular senescence in suppression of Pten-deficient tumorigenesis *Nature.* 2005; 436:725. [PubMed: 16079851]
- Chen M. Pratt CP. Zeeman ME. Schultz N. Taylor BS. O'Neill A. Castillo-Martin M. Nowak DG. Naguib A. Grace DM. Identification of PHLPP1 as a tumor suppressor reveals the role of feedback activation in PTEN-mutant prostate cancer progression *Cancer Cell.* 2011; 20:173. [PubMed: 21840483]
- Cho H. Herzka T. Zheng W. Qi J. Wilkinson JE. Bradner JE. Robinson D. Castillo-Martin M. Cordon-Cardo C. Trotman LC. RapidCaP, a novel GEM model for analysis and therapy of metastatic prostate cancer reveals Myc as a driver of Pten-mutant metastasis *Cancer Discov.* 2014; 4:318. [PubMed: 24444712]

- Cho H. Herzka T. Stahlhut C. Watrud K. Robinson BD. Trotman LC. Rapid in vivo validation of candidate drivers derived from the PTEN-mutant prostate metastasis genome *Methods*. 2015; 77–78:197.
- Ding Z. Wu CJ. Chu GC. Xiao Y. Ho D. Zhang J. Perry SR. Labrot ES. Wu X. Lis R. SMAD4-dependent barrier constrains prostate cancer growth and metastatic progression *Nature*. 2011; 470:269. [PubMed: 21289624]
- Fang N. Casida JE. Anticancer action of cube insecticide: correlation for rotenoid constituents between inhibition of NADH:ubiquinone oxidoreductase and induced ornithine decarboxylase activities *Proc. Natl. Acad. Sci. USA*. 1998; 95:3380. [PubMed: 9520374]
- Garcia J. Barluenga S. Gorska K. Sasse F. Winssinger N. Synthesis of deguelin-biotin conjugates and investigation into deguelin's interactions *Bioorg. Med. Chem*. 2012; 20:672. [PubMed: 22037048]
- Garraway LA. Lander ES. Lessons from the cancer genome *Cell*. 2013; 153:17. [PubMed: 23540688]
- Gillesen S. Gilson C. James N. Adler A. Sydes MR. Clarke N. Group, S.T.M. STAMPEDE Trial Management Group. Repurposing metformin as therapy for prostate cancer within the STAMPEDE trial platform *Eur. Urol*. 2016; 70:906. [PubMed: 27450106]
- Gundem G. Van Loo P. Kremeyer B. Alexandrov LB. Tubio JMC. Papaemmanuil E. Brewer DS. Kallio HML. Hognas G. Annala M. ICGC Prostate Group. The evolutionary history of lethal metastatic prostate cancer *Nature*. 2015; 520:353. [PubMed: 25830880]
- Kim JS. Lee C. Bonifant CL. Ransom H. Waldman T. Activation of p53-dependent growth suppression in human cells by mutations in PTEN or PIK3CA *Mol. Cell. Biol*. 2006; 27:662. [PubMed: 17060456]
- Landman GW. Kleefstra N. van Hateren KJ. Groenier KH. Gans RO. Bilo HJ. Metformin associated with lower cancer mortality in type 2 diabetes: ZODIAC-16 *Diabetes Care*. 2010; 33:322. [PubMed: 19918015]
- Margel D. Urbach D. Lipscombe LL. Bell CM. Kulkarni G. Austin PC. Fleshner N. Association between metformin use and risk of prostate cancer and its grade *J. Natl. Cancer Inst*. 2013a; 105:1123. [PubMed: 23853056]
- Margel D. Urbach DR. Lipscombe LL. Bell CM. Kulkarni G. Austin PC. Fleshner N. Metformin use and all-cause and prostate cancer-specific mortality among men with diabetes *J. Clin. Oncol*. 2013b; 31:3069. [PubMed: 23918942]
- Martínez-Reyes I. Diebold LP. Kong H. Schieber M. Huang H. Hensley T. Mehta MM. Wang T. Santos JH. Woychik R. TCA cycle and mitochondrial membrane potential are necessary for diverse biological functions *Mol. Cell*. 2016; 61:199. [PubMed: 26725009]
- Naguib A. Bencze G. Cho H. Zheng W. Tocilj A. Elkayam E. Faehnle CR. Jaber N. Pratt CP. Chen M. PTEN functions by recruitment to cytoplasmic vesicles *Mol. Cell*. 2015; 58:255. [PubMed: 25866245]
- Nowak DG. Cho H. Herzka T. Watrud K. DeMarco DV. Wang VM. Senturk S. Fellmann C. Ding D. Beinortas T. MYC drives Pten/p53-deficient proliferation and metastasis due to Il6-secretion and Akt-suppression via Phlp2 *Cancer Discov*. 2015; 5:636. [PubMed: 25829425]
- Pernicova I. Korbonits M. Metformin — mode of action and clinical implications for diabetes and cancer *Nat. Rev. Endocrinol*. 2014; 70:143.
- Robinson D. Van Allen EM. Wu YM. Schultz N. Lonigro RJ. Mosquera JM. Montgomery B. Taplin ME. Pritchard CC. Attard G. Integrative clinical genomics of advanced prostate cancer *Cell*. 2015; 767:1215.
- Rothermundt C. Hayoz S. Templeton AJ. Winterhalder R. Strebel RT. Bartschi D. Pollak M. Lui L. Endt K. Schiess R. Metformin in chemotherapy-naive castration-resistant prostate cancer: a multicenter phase 2 trial (SAKK 08/09) *Eur. Urol*. 2014; 66:468. [PubMed: 24412228]
- Seo BB. Kitajima-Ihara T. Chan EK. Scheffler IE. Matsuno-Yagi A. Yagi T. Molecular remedy of complex I defects: rotenone-insensitive internal NADH-quinone oxidoreductase of *Saccharomyces cerevisiae* mitochondria restores the NADH oxidase activity of complex I-deficient mammalian cells *Proc. Natl. Acad. Sci. U S A*. 1998; 95:9167. [PubMed: 9689052]
- Sogame Y. Kitamura A. Yabuki M. Komuro S. A comparison of uptake of metformin and phenformin mediated by hOCT1 in human hepatocytes *Biopharm. Drug Dispos*. 2009; 30:476. [PubMed: 19768675]

- Taylor BS. Schultz N. Hieronymus H. Gopalan A. Xiao Y. Carver BS. Arora VK. Kaushik P. Cerami E. Reva B. Integrative genomic profiling of human prostate cancer *Cancer Cell*. 2010; 18:11. [PubMed: 20579941]
- Therasse P. Arbuck SG. Eisenhauer EA. Wanders J. Kaplan RS. Rubinstein L. Verweij J. Van Glabbeke M. van Oosterom AT. Christian MC. Gwyther SG. New guidelines to evaluate the response to treatment in solid tumors. European Organization for Research and Treatment of Cancer, National Cancer Institute of the United States, National Cancer Institute of Canada *J. Natl. Cancer Inst.* 2000; 92:205. [PubMed: 10655437]
- Wang Y. Ma W. Zheng W. Deguelin, a novel anti-tumorigenic agent targeting apoptosis, cell cycle arrest and anti-angiogenesis for cancer chemoprevention *Mol. Clin. Oncol.* 2013; 1:215. [PubMed: 24649149]
- Wang Y. Waters J. Leung ML. Unruh A. Roh W. Shi X. Chen K. Scheet P. Vattathil S. Liang H. Clonal evolution in breast cancer revealed by single nucleus genome sequencing *Nature*. 2014; 512:155. [PubMed: 25079324]
- Wheaton WW. Weinberg SE. Hamanaka RB. Soberanes S. Sullivan LB. Anso E. Glasauer A. Dufour E. Mutlu GM. Budigner GS. Chandel NS. Metformin inhibits mitochondrial complex I of cancer cells to reduce tumorigenesis *eLife*. 2014; 3:e02242. [PubMed: 24843020]
- Xu H. Aldrich MC. Chen Q. Liu H. Peterson NB. Dai Q. Levy M. Shah A. Han X. Ruan X. Validating drug repurposing signals using electronic health records: a case study of metformin associated with reduced cancer mortality *J. Am. Med. Inform. Assoc.* 2015; 22:179. [PubMed: 25053577]

Highlights

- A screen identifies complex I inhibitors as highly selective against *Pten*-null cells
- *Pten*-null selectivity is unmatched by common standard of care chemotherapy agents
- Mitochondria of *Pten*-null cells easily switch to consuming ATP instead of producing it
- The complex I inhibitor deguelin can suppress lethal prostate cancer in RapidCaP

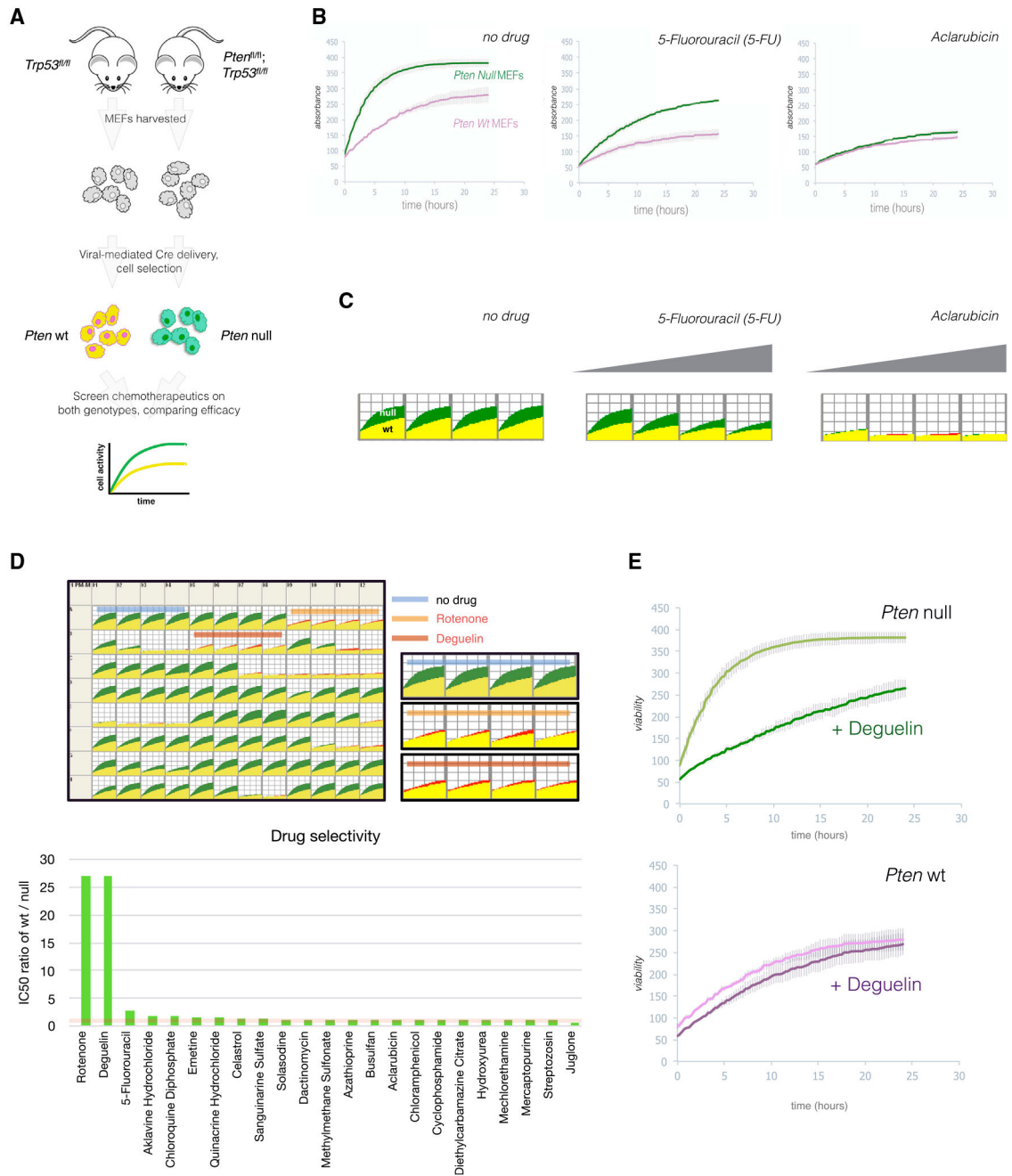


Figure 1. Identification of Chemotherapeutics with Efficacy against *Pten*-Null Genotype
 (A) Schematic of chemotherapeutic screen workflow. MEFs were harvested from mice, and cellular genomic DNA was recombined after infection with adenovirus encoding *Cre* recombinase. Cells were selected (using viral vector-encoded selection markers) to generate pure populations. Chemotherapeutic efficacy of 23 agents (each at three concentrations) was assessed, and effects on the two genotypes were measured via assessment of cell activity, viability, and number (tetrazolium dye-based assay developed by Biolog).
 (B) Viability measured over a 24 hr period of *Pten*-WT and *Pten*-null cells in the presence of four exemplary drugs. Graphs show data from two biological replicates. Error bars show SD.

(C) Biolog system output for visualization of results from (B).

(D) Top: overview of the 96-well results obtained at four concentrations per drug, with colored bars indicating location of no drug control (blue), rotenone(orange), and deguelin (red). Top right: magnification of highlighted wells. Bottom: post-screen IC_{50} calculation identifies rotenone and deguelin as hits for specific toxicity in *Pten*-null MEFs.

(E) Cell viability after deguelin treatment is measured in the Biolog system for each genotype and shows a strong effect in *Pten*-null but not *Pten*-WT cells. Graphs show data from two biological replicates. Error bars show SD

Author Manuscript

Author Manuscript

Author Manuscript

Author Manuscript

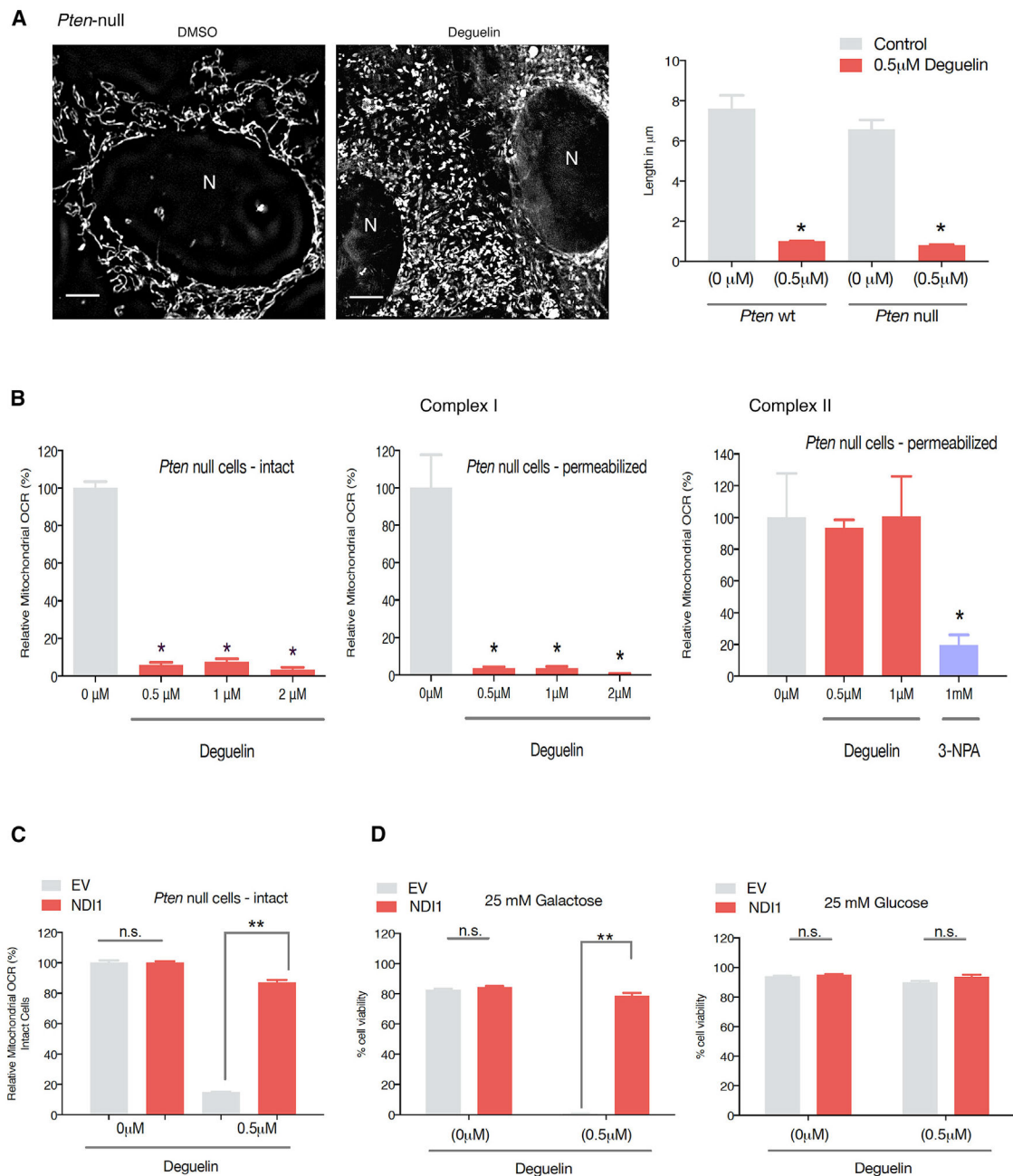


Figure 2. Deguelin Kills *Pten*-Null Cells by Targeting Mitochondrial Complex I

(A) Left: super-resolution imaging (OMX) of mitochondria stained with MitoTracker shows fragmentation induced by deguelin. Scale bars, 10 μm . Right: Quantification of mitochondrial lengths after treatment with deguelin. Note that both cell types respond to deguelin with fragmentation. Error bars show SEM ($n = 3$); one-way ANOVA with multiple comparisons test; $*p < 0.0001$. See also Figure S1C.

(B) Left: relative OCR by complex I in intact *Pten*-null MEFs normalized to DMSO-treated control cells. Middle: relative complex I OCR in saponin-permeabilized *Pten*-null MEFs. Error bars are SD, $n = 5$ replicates per group; one-way ANOVA with Dunnett multiple

comparisons; * $p < 0.0001$ compared with 0 μM deguelin. Right: relative mitochondrial complex II-driven oxygen consumption rate of saponin-permeabilized *Pten*-null MEFs in the presence of deguelin or the complex II inhibitor 3-nitropropionic acid (3-NPA) and normalized to DMSO-treated control cells. Error bars are $\pm\text{SEM}$ ($n = 3$ independent experiments); one-way ANOVA with Dunnett multiple comparisons; * $p < 0.05$ compared with 0 μM deguelin.

(C) Relative mitochondrial oxygen consumption rate (OCR) of intact p53/pTen^{-/-} MEFs stably expressing either the empty vector (EV) or the yeast NDI1 gene was measured in the presence of 0.5 μM deguelin using the Seahorse Biosciences XF24 Extracellular Flux Analyzer and normalized to the corresponding untreated cells. Error bars are SEM ($n = 3$ independent experiments); one-way ANOVA with Bonferroni multiple comparisons; ** $p < 0.0001$.

(D) *Pten*-null cells stably expressing either the EV or the yeast NDI1 gene were cultured in media containing 25 mM galactose and treated with or without 0.5 μM deguelin for 24 hr. Error bars are SEM ($n = 3$ independent experiments); two-way ANOVA with Bonferroni multiple comparisons; ** $p < 0.0001$.

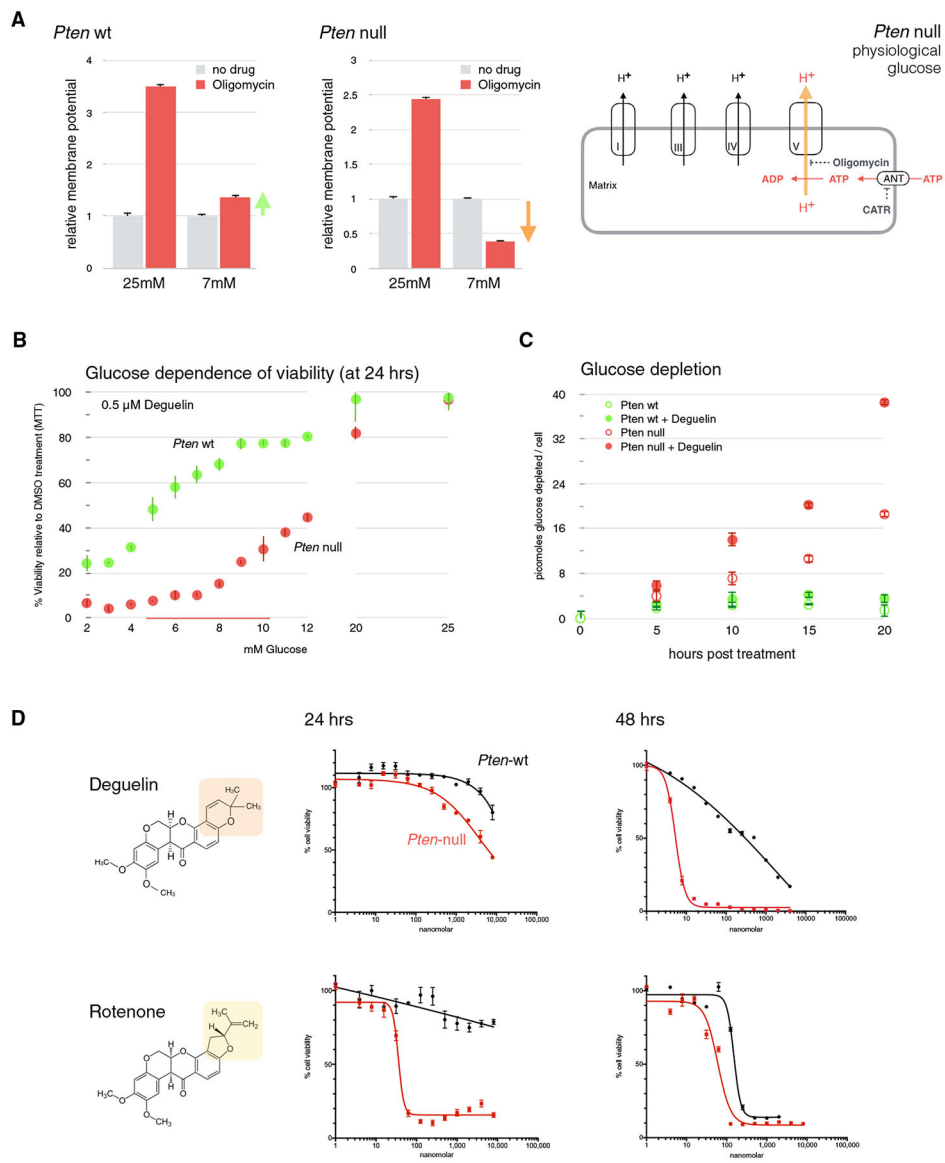


Figure 3. Complex V Function Is Reversed in *Pten*-Null Cells

(A) Relative mitochondrial membrane potential of cells grown in 25 or 7 mM glucose and in the presence or absence of the complex V inhibitor oligomycin. *Pten*-WT cells show increased membrane potential upon oligomycin treatment at physiological glucose. In contrast, *Pten*-null cells show decreased membrane potential under these conditions, demonstrating reversed proton flow through complex V. Right: schematic of reversed complex V function and its inhibition by oligomycin, resulting in decreased membrane potential because complex V is exporting protons at the cost of ATP consumption. Error bars are SD (n = 8). See also Figures S2D and S2E.

(B) MTT assay for viability upon deguelin treatment as a function of glucose concentration and *Pten* status. A red line on the x axis indicates physiological glucose range. Error bars are SD (n = 3).

(C) Per cell glucose consumption in *Pten*-null or WT cells in the presence or absence of 0.5 μ M deguelin. *Pten*-null cells treated with deguelin showed an increased dependence on glucose consumption compared with untreated. Error bars are SD (n = 3).

(D) *Pten*-null and *Pten*-WT cells were grown in 7 mM glucose, and kill curves were determined for deguelin and rotenone at 24 and 48 hr post-treatment. Error bars are SD (n = 4).

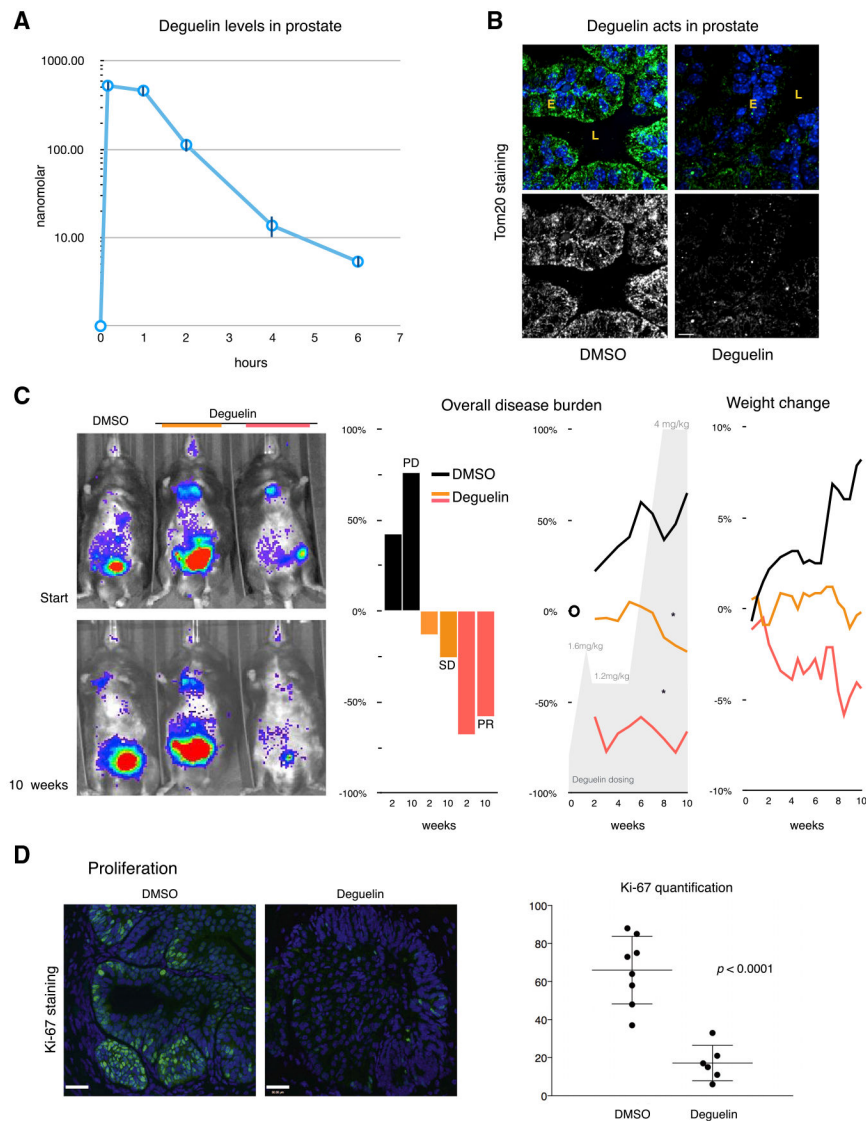


Figure 4. Deguelin Can Be Used to Target Lethal Prostate Cancer

(A) LC-MS analysis of deguelin concentration in the prostate at up to 6 hr post-intra-peritoneal (i.p.) injection.

(B) Staining of mitochondrial Tom20 in prostate tissue from deguelin-treated WT animals shows a loss of staining compared with untreated tissue (see also Figure S3C). E denotes location of the prostatic epithelium and L that of the prostatic lumen; see also Figure S3B. Scale bar, 10 μ m.

(C) Left: percentage change in bioluminescence luciferase imaging (BLI) of DMSO- or deguelin-treated mice at start and end of the 10 week trial. Middle: waterfall plot for overall disease burden as measured by relative change to starting BLI at 2 and 10 weeks, respectively. Line graph for overall disease burden, measured by relative percentage BLI signal change from start shows significant differences between control and treatment animals. The dosing increase from 0.4 to 4 mg/kg during the 10week period is indicated in gray; see also Figure S3D. Lines show moving averages (period = 3), and asterisks indicate

$p < 0.05$ after linear regression analysis compared with DMSO. Linear regression analysis was performed on the full dataset, not the moving average. Right: deguelin was well tolerated, as judged by minor changes in relative body weight over the 10 week trial period. (D) Absence of abnormal proliferation, as judged by Ki-67 staining of prostate tissue from deguelin-treated mouse B confirms successful suppression of disease. Scale bars, 30 μm . Quantification shows percentage Ki-67 positive nuclei per gland. Error bars are SEM; unpaired t test (control, $n = 8$; treated, $n = 6$).